

## DEEP HUBBLE SPACE TELESCOPE WFPC2 PHOTOMETRY OF M31'S THICK DISK (?)

ATA SARAJEDINI<sup>1</sup>

Department of Astronomy, University of Florida, P.O. Box 112055, Gainesville, FL 32611-2055; ata@astro.ufl.edu

AND

JEFFREY VAN DUYNÉ<sup>2</sup>

Department of Astronomy, Wesleyan University, Middletown, CT 06459; jeff@astro.wesleyan.edu

Received 2001 June 26; accepted 2001 July 16

### ABSTRACT

We present deep color-magnitude diagrams (CMDs) for a field along the outer disk of M31 based on archival *Hubble Space Telescope* Wide Field Planetary Camera 2 observations in the F555W ( $\sim V$ ) and F814W ( $\sim I$ ) filters. The CMDs, which contain a total of about 50,000 stars, feature a prominent red giant branch (RGB) along with a significant population of helium-burning red clump stars. In addition, they exhibit the rarely seen asymptotic giant branch clump, as well as a weak Population II horizontal branch. There is also the hint of a  $\sim 2$  Gyr subgiant branch at the faintest levels of the CMDs. After adopting an M31 distance of  $(m - M)_0 = 24.5$  and a reddening of  $E(B - V) = 0.08$ , we draw the following conclusions. (1) The  $I$ -band absolute magnitude of the helium-burning red clump stars is  $M_I(\text{RC}) = -0.29 \pm 0.05$ , which is in accord with the value derived from *Hipparcos* parallaxes of solar neighborhood clump stars by Stanek & Garnavich. (2) The metallicity distribution function constructed from bright RGB stars shows a characteristic shape; however, a pure halo population consisting of metal-poor and intermediate-metallicity components (as advocated in the literature) is not sufficient to account for this shape. Instead, an additional Gaussian component with  $\langle [\text{Fe}/\text{H}] \rangle = -0.22 \pm 0.26$ , comprising 70% of the total number of stars, is required. (3) A comparison of our CMD with theoretical isochrones indicates that the majority of stars in our M31 field have ages that are  $\gtrsim 1.5$  Gyr. (4) These points, along with the physical location of our field in M31, suggest that we are observing the thick-disk population of this galaxy.

*Key words:* color-magnitude diagrams — galaxies: individual (M31) — Local Group — stars: abundances

### 1. INTRODUCTION

The determination of star formation histories for spiral galaxies is an important ingredient in constraining models of galaxy formation (Bullock 1999; Grebel 2000; Silk 2001). The three most readily available subjects are, of course, our own Milky Way galaxy, M31, and M33. Being within the Milky Way makes much of this work difficult, which is why a good understanding of the disk and halo of M31 is so important. However, little is known about the early star formation history of M31 due primarily to the lack of sufficiently deep photometry of its disk and halo.

There is a rich history of ground-based work dealing with the stellar populations of M31. The reader is referred to the review by van den Bergh (1999) for a discussion of many of these results. For the purposes of the present paper, we concentrate on previous photometric investigations of the outer disk and inner halo. We begin by noting that ground-based photometry has only generated color-magnitude diagrams (CMDs) of M31 field stars as deep as the horizontal branch, which is roughly at  $I = 24.5$  (Durrell, Harris, & Pritchet 1994). Nevertheless, a great deal can be learned about M31 by examining the colors and magnitudes of the brighter stars.

Pritchet & van den Bergh (1988) present photometry for an inner halo field located 40' southeast of the nucleus along the minor axis. They find a mean abundance of  $[\text{Fe}/\text{H}] \sim -1.0$ , similar to the Galactic globular NGC 6171, with a dispersion of  $\sim 0.3$  dex. The work of Davidge (1993) on an inner halo field situated on the opposite side of the galaxy near NGC 205 confirms these results; namely, he finds a mean  $[\text{Fe}/\text{H}]$  between  $-1.3$  and  $-0.7$  along with a metallicity dispersion of  $\sim 0.3$  dex. Davidge (1993) also presents observations that sample the outer disk of M31 at a location 25.6 from the nucleus. As one would expect, this field presents a rather complicated stellar population profile, suggesting a significant range in age and metallicity among the stars. Previously, Hodge & Lee (1988; see also Hodge, Lee, & Mateo 1988 and Massey, Armandroff, & Conti 1986) imaged six disk fields in M31 and were able to study reddening variations in their fields along with the properties of the luminosity functions. The color-magnitude diagrams published by Richer, Crabtree, & Pritchet (1990) and Morris et al. (1994) reveal the metal-rich nature of the M31 disk. The latter study finds a mean metal abundance that is significantly higher than that of 47 Tuc ( $[\text{Fe}/\text{H}] = -0.7$ ). Recent wide field imaging observations of M31's outer disk by Cuillandre et al. (2001) are used to investigate the correlation between the young star population, H I column density, and the dust content.

Extending the ground-based studies with the *Hubble Space Telescope* (*HST*) has resulted in CMDs that reach 2–3 mag fainter than the M31 field horizontal branch. In spite of this, *HST* has been used relatively sparingly in

<sup>1</sup> Guest User, Canadian Astronomy Data Centre, which is operated by the Herzberg Institute of Astrophysics, National Research Council of Canada.

<sup>2</sup> Current address: Department of Astronomy, Yale University, P.O. Box 208101, New Haven, CT 06520-8101.

examining the field halo and disk populations of M31 (Holland, Fahlman, & Richer 1996; Rich, Mighell, & Neill 1996). Instead, the majority of *HST* photometry of M31 has been directed at the star clusters (Fusi Pecci et al. 1996; Holland et al. 1996; Jablonka et al. 2000).

One of these *HST* programs (GO-5420) was designed to construct CMDs of M31 star clusters using broadband filter observations with the Wide Field and Planetary Camera 2 (WFPC2). One object on the target list was intended to be the M31 globular cluster G272 ( $\alpha_{2000.0} = 00^{\text{h}}44^{\text{m}}14^{\text{s}}.5$ ,  $\delta_{2000.0} = 41^{\circ}19'19''.8$ ). Apparently however, a bright nearby star was imaged instead ( $\alpha_{2000.0} = 00^{\text{h}}44^{\text{m}}47^{\text{s}}.7$ ,  $\delta_{2000.0} = 41^{\circ}18'48''$ ). As a result, the WFPC2 observations of this field were apparently ignored and do not appear in any of the subsequent analysis papers which focus mainly on the clusters (Fusi Pecci et al. 1996).

Having come across these images in the *HST* archive and realizing that the exposure times were extraordinarily long (§ 2), the scientific utility of these observations became apparent. As discussed in § 2, this region of M31 samples both the disk and halo stellar populations. The next section

describes the observations and data reduction. Section 3 presents the resulting CMDs and the properties of the field that can be determined therein, such as the magnitude of the red clump and the metallicity distribution function. This section also contains the results of our artificial-star experiments, further analysis of the populations and their properties, and discussions of our results. Section 4 presents our conclusions and suggestions for future work.

## 2. OBSERVATIONS AND DATA REDUCTION

Our field center is situated at  $\alpha_{2000.0} = 00^{\text{h}}44^{\text{m}}50^{\text{s}}.6$  and  $\delta_{2000.0} = +41^{\circ}19'11''.1$ , which is positioned at a  $\sim 45^{\circ}$  angle from the minor axis of the M31 disk, as seen in Figure 1*a*. Figure 1*b* is an expanded view of this area, showing the *HST*-WFPC2 orientation on the sky. A scale conversion from arcminutes to kiloparsecs at our adopted M31 distance of 790 kpc (Da Costa et al. 2000; Durrell, Harris, & Pritchett 2001) places our field at a projected distance of 5.5 kpc from the center of M31.

We obtained the processed images of the G272 field from the Canadian Astronomy Data Centre. The observations

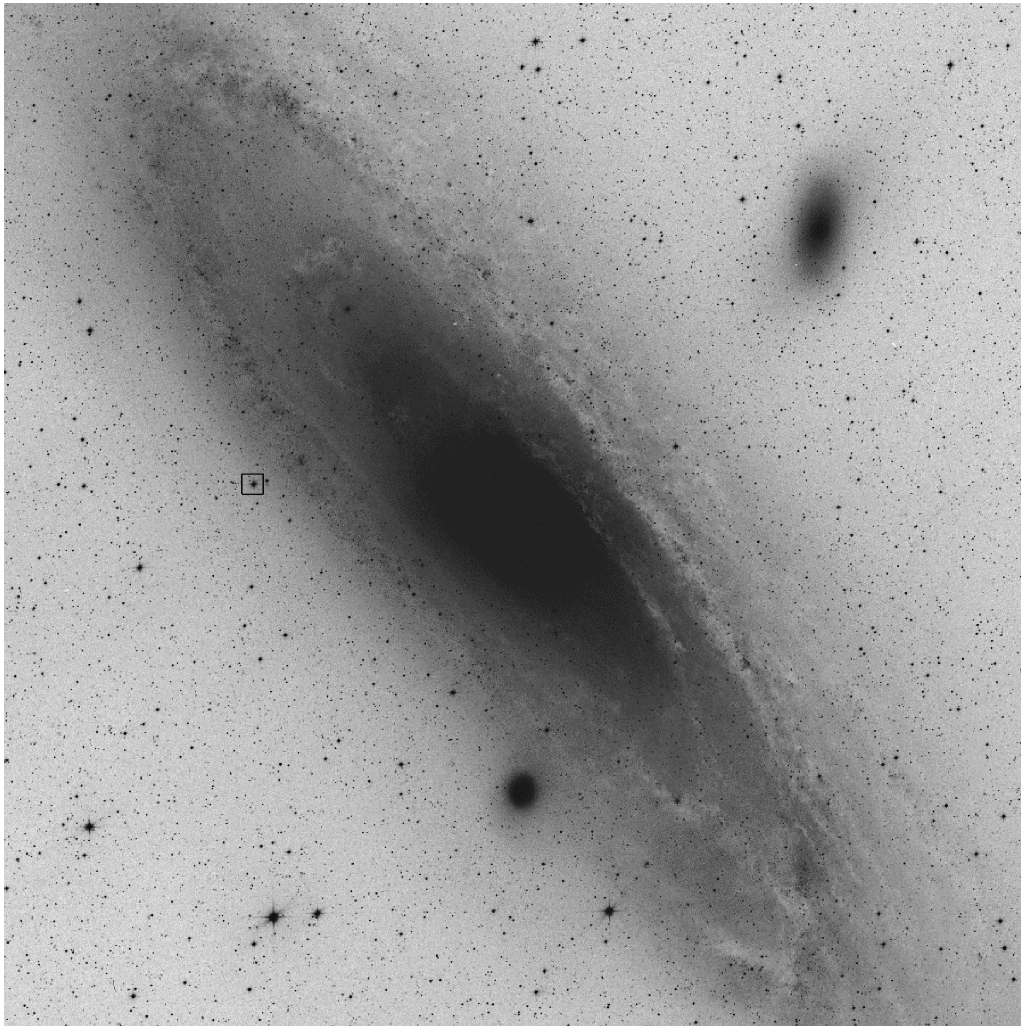


FIG. 1*a*

FIG. 1.—(a) Location of our *HST*/WFPC2 field indicated by the square in this  $1^{\circ}5' \times 1^{\circ}5'$  digitized sky survey image of M31. North is up, and east to the left. (b) Close-up view of the G272 field with the WFPC2 footprint overlaid. (c) Mosaicked WFPC2 image with the “compass” markings showing the direction of north (arrow) and east. The black lines show the three radial regions into which the photometry has been divided; region 1, which is closest to the M31 nucleus, is on the right-hand side.

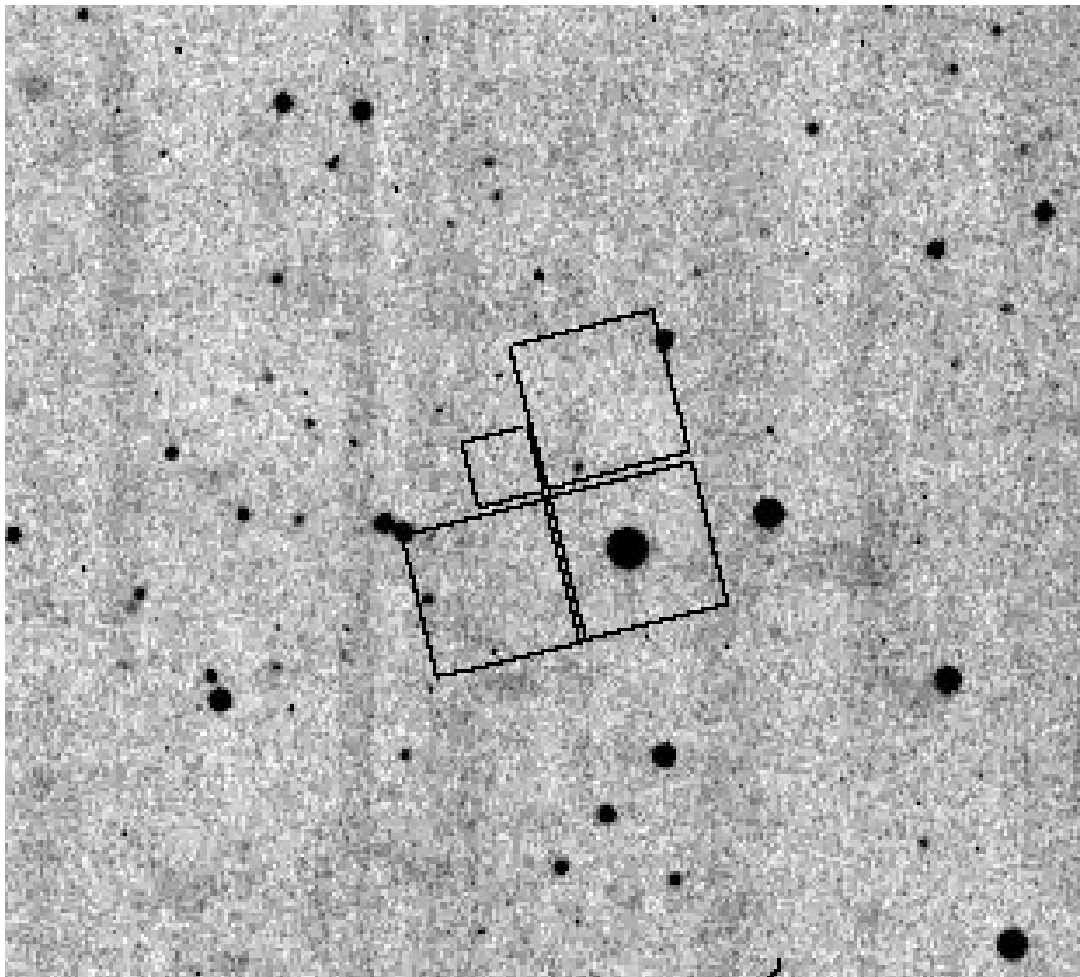


FIG. 1b

were taken on 1995 January 23 and include two frames taken in the F555W ( $\sim V$ ) filter and five taken with the F814W ( $\sim I$ ) filter, with total exposure times of 3800 and 10,800 s, respectively. The Wide Field 3 chip was ignored because of the extreme saturation effects of the foreground star, as is clearly seen in Figure 1c. Table 1 provides more detailed information about the observations.

The photometric reduction was performed on the three remaining chips (PC1, WF2, and WF4), in a manner similar to the procedure described in Sarajedini et al. (2000), utilizing the DAOPHOT II/ALLSTAR/ALLFRAME (Stetson 1994) profile fitting software. The reader is referred to that paper for details. In summary, high single-to-noise

WFPC2 F555W and F814W point-spread functions (PSFs), kindly provided by P. Stetson, were fitted to all detected profiles on each individual image using the ALLFRAME software. The resultant instrumental magnitudes were edited and matched to form colors. Aperture corrections were applied as described in the next paragraph to bring the total magnitudes to a  $0''.5$  radius. Then, a correction for the well-known charge transfer efficiency (CTE) problem was applied (Sarajedini et al. 2000) and standard magnitudes were calculated using the equations of Silbermann et al. (1996). These describe the photometric system established by the *HST* Key Project on the Cepheid distance scale and are coupled to the PSFs we used earlier in the reduction procedure.

The only departure from the procedure adopted by Sarajedini et al. (2000) was in the determination of the aperture corrections for the PC1 chip. Because of the lack of sufficient numbers of bright stars in the Planetary Camera, we adopt the following procedure to ensure consistency between the photometric scales of the three CCDs. We derived and applied aperture corrections to the WF2 and WF4 data as described by Sarajedini et al. (2000). Then, under the assumption that the spatially adjacent regions of the three chips feature the same peak magnitude for the red clump (see Figs. 1 and 2), we offset the photometry from each chip to match the average peak red clump magnitude of the WF photometry. The offsets to the WF data (0.03

TABLE 1  
OBSERVING LOG

Data Set	Filter	Exp. Time (s)
u2gv0401 .....	F555W	1500
u2gv0402 .....	F555W	2300
u2gv0403 .....	F814W	2300
u2gv0404 .....	F814W	2300
u2gv0405 .....	F814W	2300
u2gv0406 .....	F814W	2300
u2gv0407 .....	F814W	1600

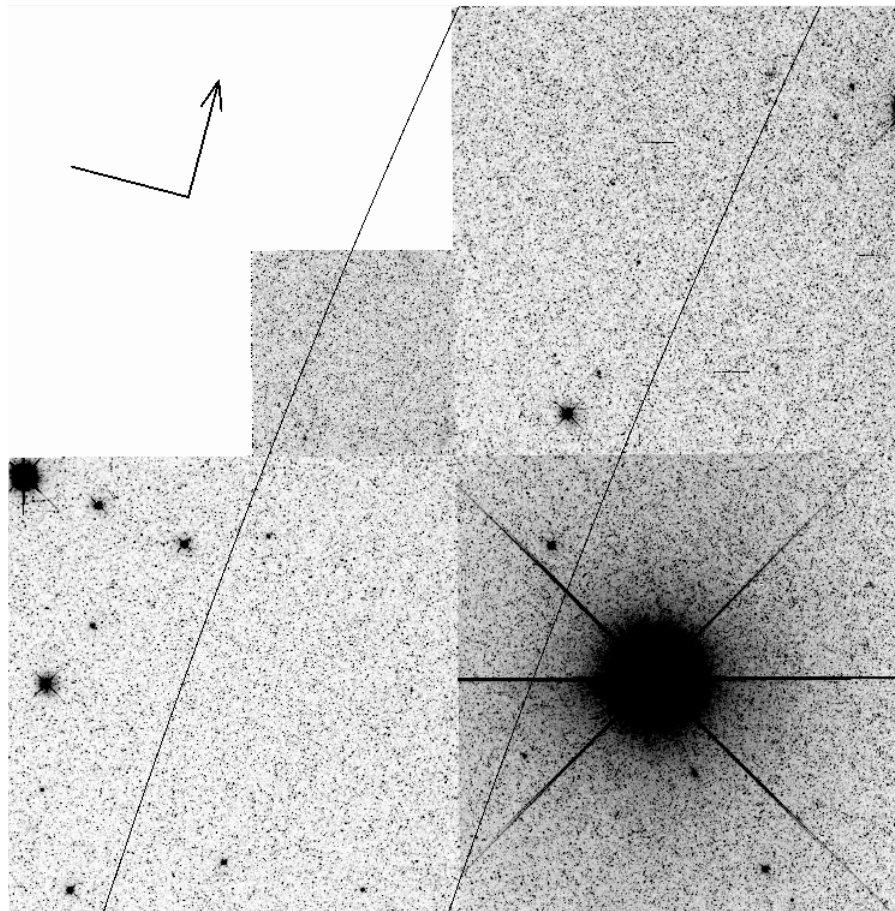


FIG. 1c

mag in  $V$  and 0.04 in  $I$ ) correct systematic offsets between the photometric scales of these two CCDs and the offsets to the PC1 data (0.03 mag in  $V$  and  $I$ ) account for the fact that no aperture corrections were applied. In any case, after the application of these offsets, we estimate that the photometric scales of the three CCDs are consistent to within  $\pm 0.015$  mag.

### 3. RESULTS AND DISCUSSION

#### 3.1. Color-Magnitude Diagrams

The left panels of Figures 2a through 2c show the color-magnitude diagrams (CMDs) of the PC1 (5249 stars), WF2 (22,793 stars), and WF4 (20,943 stars) fields, respectively, in the apparent ( $V, V-I$ ) plane, while the right panels show the same fields in the ( $I, V-I$ ) plane. The two most prominent features in these CMDs are the well-populated red giant branch (RGB), which exhibits a large range in color and an obvious red clump at  $V \sim 25.5$  and  $I \sim 24.3$ . There is also a hint of a Population II horizontal branch located blueward of the red clump extending from  $V-I \sim 0.1$  to  $V-I \sim 0.7$  with  $V \sim 25.4$  and appearing most prominently in the WF2 CMD. This feature is likely to be associated with the relatively small metal-poor population present in our field, as discussed in § 3.6. The tip of the first ascent RGB appears to be at  $I \sim 21.8$ . All of the CMDs also feature a main sequence (MS) of young stars with ages between  $10^8$  and  $10^9$  years (see below). Note also the existence of what appears to be a subgiant branch developing at

$V \sim 26.5$  (see Fig. 12 and the discussion in § 3.7). Lastly, there is a clump of stars at  $V \sim 24.7$  and  $I \sim 23.2$ , which we tentatively identify with the asymptotic giant branch (AGB) clump (Gallart 1998).

To investigate radial variations in the CMDs, we divided our sample into three regions (1, 2, and 3) based on radial distance from the center of M31. Each star's right ascension and declination was determined using the IRAF<sup>3</sup> routine METRIC and then separated into three  $1'$  (projected) wide regions. The black lines in Figure 1c show these divisions; region 1, which is closest to the M31 nucleus, is on the right-hand side of this figure.

#### 3.2. Distance and Reddening

The reddening of our M31 field was estimated using the Burstein & Heiles (1982) maps. At the location of our field ( $l = 121.60$ ,  $b = -21.53$ ), these maps indicate a reddening of  $E(B-V) = 0.08$ , which is consistent with the value used by Holland, et al. (1996). We adopt the relations  $E(V-I) = 1.25E(B-V)$  and  $A_I = 1.48E(V-I)$  from Schlegel, Finkbeiner, & Davis (1998) for the *HST* filters utilized herein.

<sup>3</sup> IRAF is distributed by the National Optical Astronomy Observatories, which are operated by the Association of Universities for Research in Astronomy, Inc., under cooperative agreement with the National Science Foundation.

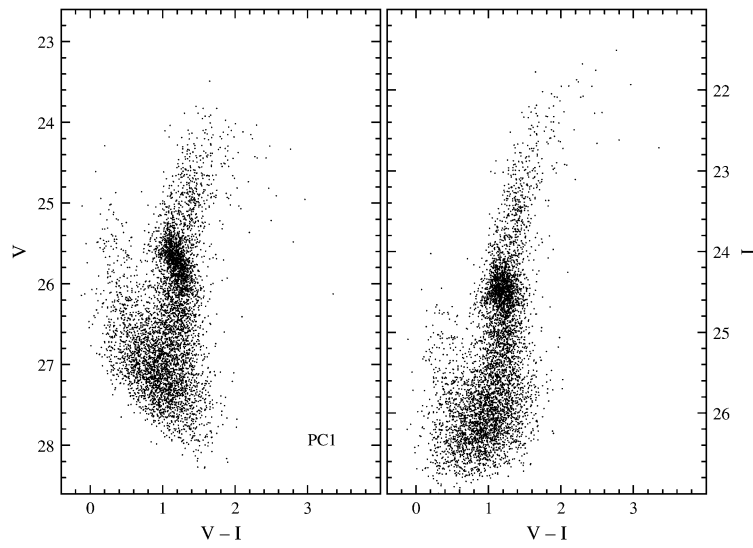


FIG. 2a

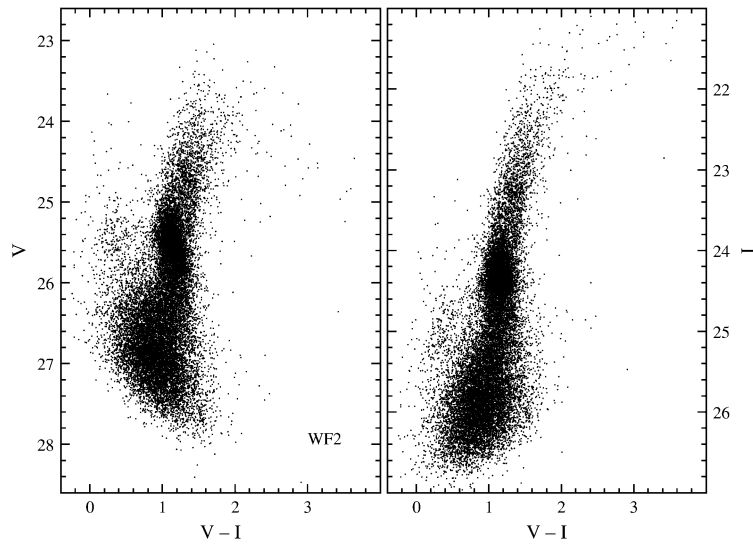


FIG. 2b

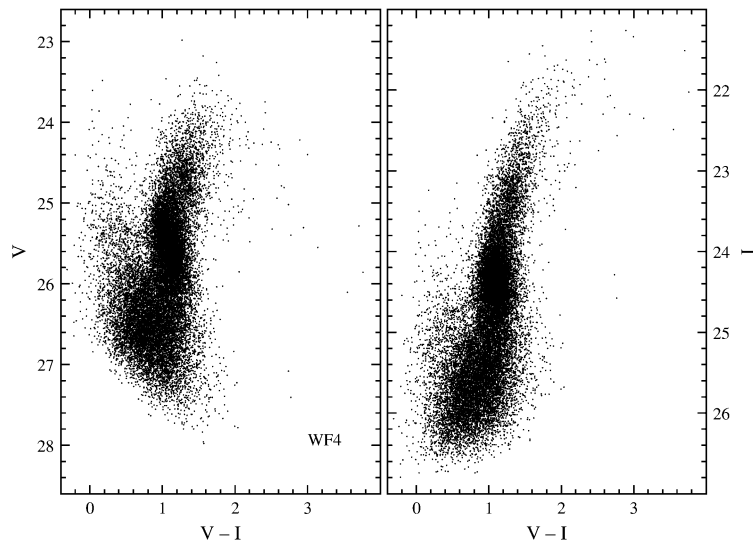


FIG. 2c

FIG. 2.—(a) Left panel shows  $(V, V-I)$  color-magnitude diagram (CMD) of the PC1; the right panel shows  $(I, V-I)$  CMD (right). (b) Same as (a) except that the WF2 CMDs are shown. (c) Same as (a) except that the WF4 CMDs are shown.

It is important to point out at this juncture that we have deliberately neglected the effects of differential reddening across our field and along the line of sight. Differential reddening due to the Galactic foreground across our (small) WFPC2 field of view is likely to be negligible. However, the effects of dust internal to M31 may have a significant effect on our results. We return to this point in § 3.6.

For the distance modulus of M31, we adopt a value of  $(m - M)_0 = 24.5 \pm 0.1$  based on the mean of those presented by Da Costa et al. (2000), who quote distances to M31 based on the field halo RR Lyraes and giant stars as well as the M31 globular clusters. This distance modulus is on the scale of Da Costa & Armandroff (1990, hereafter DCA). Figures 3a, 3b, and 3c depict our distance and reddening-corrected CMDs for the three radial regions defined above. We note that the appearance of the three CMDs is qualitatively indistinguishable.

A particularly striking feature is that the tip of the RGB, at  $M_I \sim -3$ , is significantly fainter in all three CMDs than the canonical value of  $M_I = -4.05 \pm 0.10$  (DCA; Sakai, Zaritsky, & Kennicutt 2000; Bellazzini, Ferraro, & Pancino 2001). In contrast, the RGB tip is easily identified at  $I \sim 20.6$  ( $M_I \sim -4.0$ ) in Figure 2 of Holland et al. (1996) showing the CMD of the field around the M31 globular cluster G302 constructed from *HST* observations similar to those considered herein. The faintness of the RGB tip is consistent with the fiducials of very metal-rich star clusters such as NGC 6553 and NGC 6528 (Bica, Barbuy, & Ortolani 1991), giving us our first hint that this field in M31 contains a very metal-rich stellar population. More discussion of this phenomenon is provided in § 3.4.

### 3.3. Horizontal Branch and Red Clump

As mentioned above, the most conspicuous feature of the M31 field star CMD presented herein is the helium-burning red clump (RC). Based on Figure 3, we find peak values of  $M_I(\text{RC}) = -0.28 \pm 0.05$ ,  $-0.30 \pm 0.05$ , and  $-0.29 \pm 0.05$  for regions 1, 2, and 3, respectively. All of these values are identical to within the errors and very close to the red clump absolute magnitude advocated by Stanek & Garnavich (1998); they find  $M_I(\text{RC}) = -0.23 \pm 0.03$  based on *Hipparcos* parallaxes of solar neighborhood red clump stars.

Not so conspicuous but nevertheless present in the CMDs is a Population II horizontal branch most easily seen in the CMD of region 1 shown in Figure 3a. The location of this feature is evident in Figure 4 where we have superposed the HBs and RGBs of the well-known Galactic globular clusters M68 (Walker 1994) and M5 (Johnson & Bolte 1998). The metallicities, distance moduli, and reddenings for these clusters are taken from Table 1 of Layden & Sarajedini (1997) adopting  $A_V = 3.1E(B - V)$ .

### 3.4. Asymptotic Giant Branch

As already noted, the CMDs of the G272 field show evidence for the AGB clump. Analogous to the RGB clump (Fusi Pecci et al. 1990; Sarajedini & Forrester 1995; Ferraro et al. 1999), the AGB feature is caused by a temporary pause in the evolution of stars as they proceed up the AGB and is related to the formation of the helium-burning shell (Caputo et al. 1989). As shown by Alves & Sarajedini (1999), the luminosity of the AGB clump (alternatively referred to as the AGB bump because of its appearance in a luminosity function) is primarily a function of the mean age

and metal abundance of the stellar population. To eliminate the effects of distance uncertainties, the magnitude of the AGB bump is measured relative to the horizontal branch/red clump [ $\Delta V(\text{AGBC} - \text{RC})$ ].

Building upon the work of Castellani, Chieffi, & Pulone (1991) and Ferraro (1992), Alves & Sarajedini (1999) present  $\Delta V(\text{AGBC} - \text{RC})$  values for four Galactic globular clusters—M5, NGC 1261, NGC 2808, and 47 Tuc—the only ones in which the AGB could be isolated at the time. They showed that the predictions of the theoretical models are in good agreement with the ages, metallicities, and  $\Delta V(\text{AGBC} - \text{RC})$  values of these clusters.

For our M31 field, we have already measured the luminosity of the red clump and thus adopt  $M_I(\text{RC}) = -0.29 \pm 0.05$  as the mean of the three regions shown in Figure 3. The average color of the red clump is  $(V - I)_0 = 1.00 \pm 0.05$  making the absolute  $V$  magnitude of the red clump equal to  $M_V(\text{RC}) = 0.71 \pm 0.07$ . Performing the same calculation on the AGB clump stars, we find  $M_V(\text{AGBC}) = -0.10 \pm 0.07$ , leading to a difference of  $\Delta V(\text{AGBC} - \text{RC}) = -0.81 \pm 0.10$ . Assuming that the G272 field is not significantly older than the Galactic globulars, Figure 6 of Alves & Sarajedini (1999) suggests that the metal abundance of this field is likely to be greater than about  $-0.4$  dex. However, because the Alves & Sarajedini models do not extend to more metal-rich regimes, it is difficult to say anything more definitive. In any case, we have once again confirmed the metal-rich nature of the stellar population in the G272 field.

### 3.5. Artificial-Star Experiments

As noted above, the RGB shows a rather large color width; one of the factors that could influence this width is the photometric error. In order to assess its importance, we performed a number of artificial-star experiments. These consist of placing stars of known magnitude and color on our original CCD frames and applying the same reduction techniques as those used in the reduction of the genuine stars. We placed these stars on each frame arranged in a grid pattern under the constraint that no two artificial stars were within 2 PSF radii of each other. The resultant images were reduced using the same method described in § 2. Four trials were performed with a total of 1668 stars recovered after reducing the three CCDs. The magnitudes of the artificial stars were taken from a locus with  $22.55 < I < 24.95$  along the RGB as displayed in Figure 5a. The locations of the stars at their recovered magnitudes and colors are shown by the points in Figure 5a. The difference between the input and measured colors is shown in Figure 5b as a function of the apparent  $I$  magnitude.

To determine the photometric error along the RGB, we fitted a Gaussian curve to the color distribution of artificial stars with  $22.55 \leq I \leq 22.75$  (Fig. 5c). As discussed in the next section, we have chosen to use the brighter RGB stars to study the metallicity distribution of this field. Thus, at  $I = 22.65$ , which corresponds to  $M_I = -2$  using our adopted distance modulus of  $(m - M)_I = 24.65$ , the artificial stars exhibit a standard deviation of  $\sigma_{\text{err}} = 0.049$  in  $V - I$ . This quantity is taken to be the mean photometric error at this magnitude (i.e.,  $I = 22.65$ ,  $M_I = -2$ ) and will be used in the metal abundance analysis of the next section.

The bottom panel of Figure 6 shows our actual photometry in the distance- and reddening-corrected CMD, and the solid lines are the RGBs of M15 (*left*) and NGC 6791 (*right*), which encompass the majority of RGB stars; the

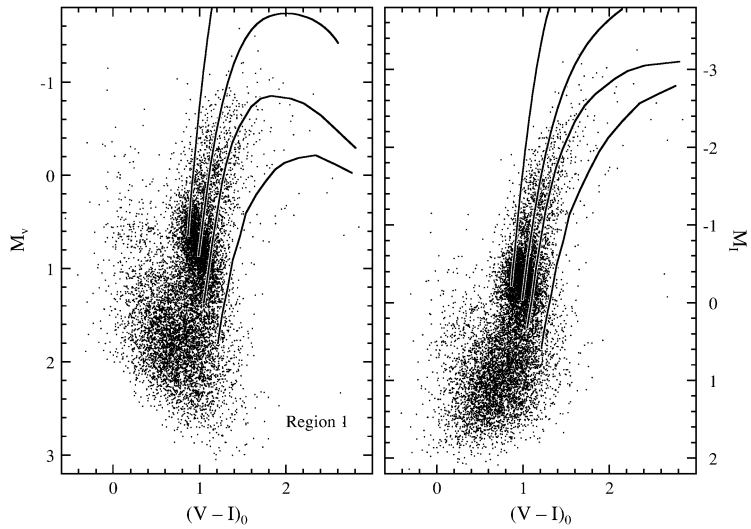


FIG. 3a

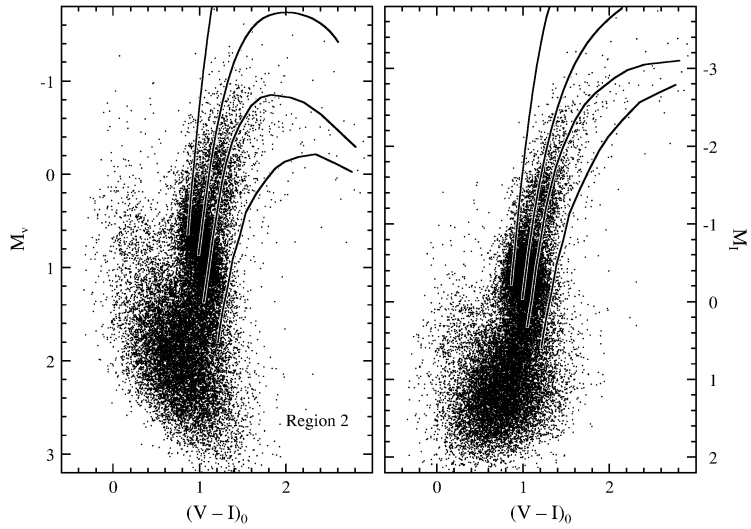


FIG. 3b

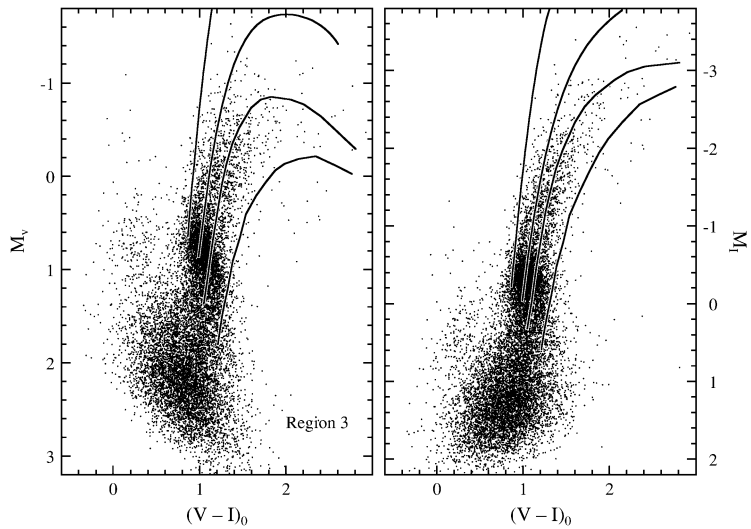


FIG. 3c

FIG. 3.—(a) Left panel shows the distance and reddening corrected  $[M_V, (V-I)_0]$  color-magnitude diagram (CMD) for region 1 assuming  $(m-M)_0 = 24.5$  and  $E(B-V) = 0.08$ ; the right panel shows the  $[M_I, (V-I)_0]$  CMD. The solid lines are the red giant branches of M15, 47 Tuc, NGC 6553, and NGC 6791. (b) Same as (a) except that the region 2 CMDs are shown. (c) Same as (a) except that the region 3 CMDs are shown.

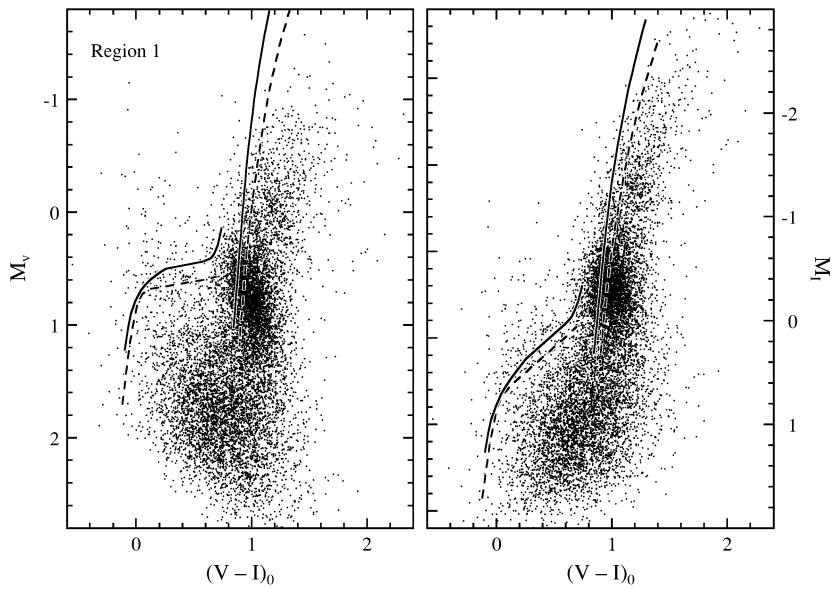


FIG. 4.—*Left*: Distance and reddening corrected  $[M_V, (V-I)_0]$  color-magnitude diagram (CMD) for region 1. *Right*:  $[M_I, (V-I)_0]$  CMD. The solid lines are the red giant and horizontal branches of M68 and the dashed lines are those of M5. This comparison is designed to illustrate the presence of a Population II horizontal branch in our M31 field.

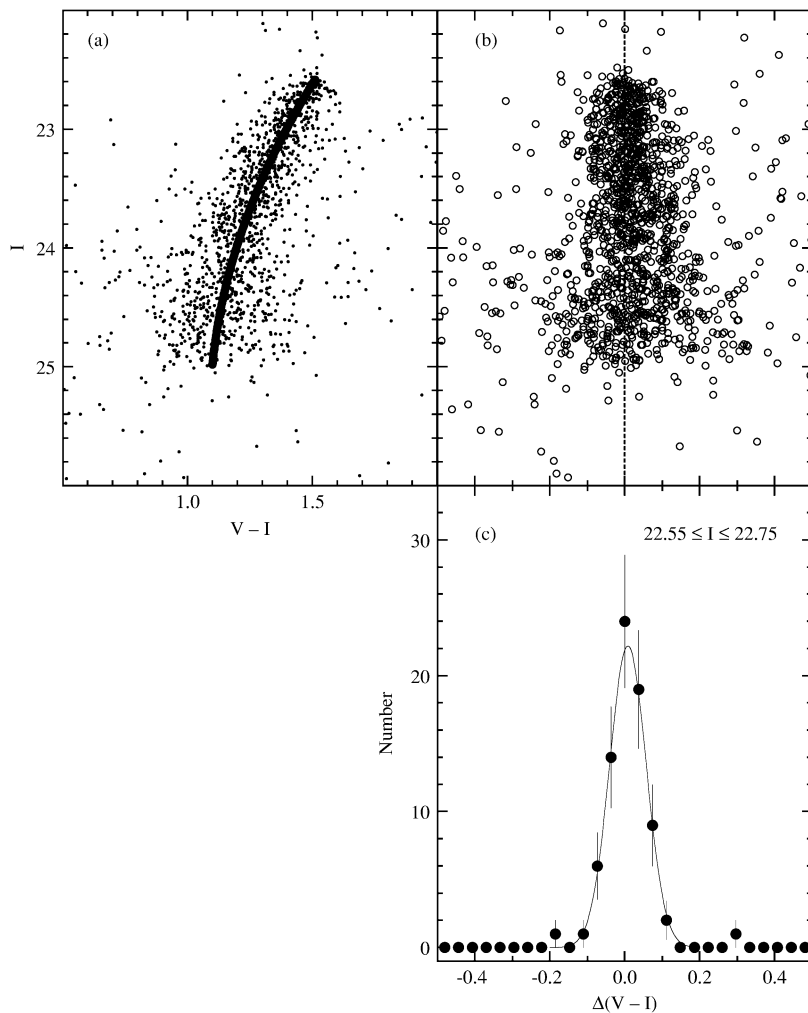


FIG. 5.—Results of the artificial-star experiments. (a) The solid sequence represents the red giant branch of artificial stars placed on the images while the points show the locations of stars after they have been measured using our photometric technique. (b) Open circles illustrate the difference between the measured and actual  $V-I$  colors  $[\Delta(V-I)]$  of the artificial stars as a function of  $I$  magnitude. (c) For all artificial stars in the magnitude range  $22.55 \leq I \leq 22.75$ , we show the histogram of  $\Delta(V-I)$  values with the fitted Gaussian distribution as the solid line. The standard deviation of this Gaussian is 0.049 mag, which we adopt as the photometric error in this magnitude range.

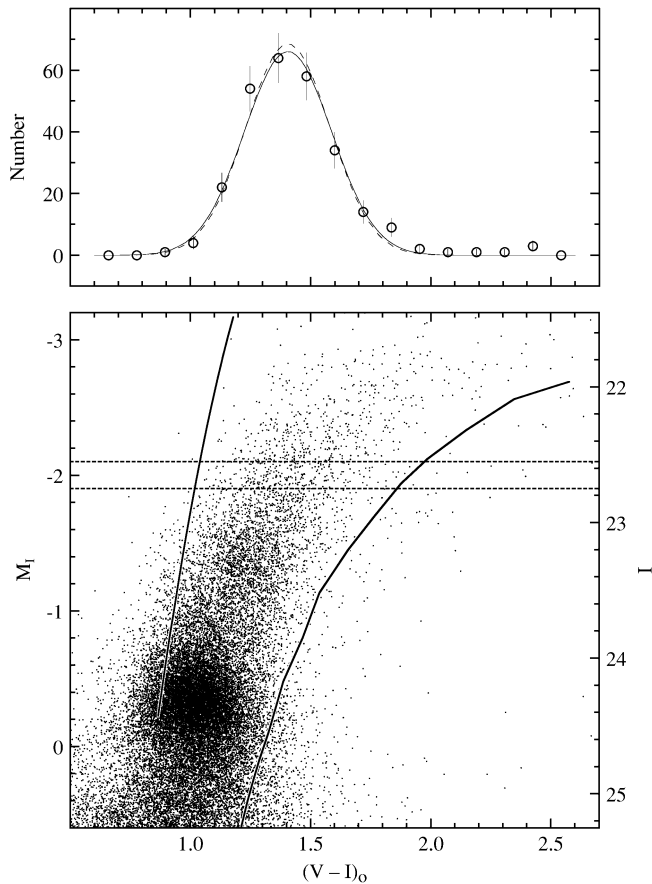


FIG. 6.—*Bottom*: Distance and reddening corrected CMD of our M31 field along with the red giant branches of M15 (*leftmost*) and NGC 6791 shown as the solid lines. The two horizontal dashed lines indicate the magnitude range over which the color histogram in the top panel has been constructed. The solid line in the top panel is a Gaussian with  $\sigma_{\text{obs}} = 0.182$  mag fitted to this histogram. Given that the photometric error in this magnitude range is  $\sigma_{\text{err}} = 0.049$  mag as yielded by the artificial stars, this implies an intrinsic color dispersion of  $\sigma_{\text{int}} = 0.175$  mag represented by the dashed Gaussian (*top*).

dotted lines enclose the magnitude range  $-2.1 \leq M_I \leq -1.9$  ( $22.55 \leq I \leq 22.75$ ) over which the color histogram shown in the top panel has been constructed. The solid line in the top panel shows the weighted least-squares fit of a Gaussian function to this distribution. The standard deviation of this fit is  $\sigma_{\text{obs}} = 0.182$ , which is much larger than the contribution purely from the photometric error. In fact, if we subtract  $\sigma_{\text{err}}$  from  $\sigma_{\text{obs}}$  in quadrature, we find an intrinsic color spread of  $\sigma_{\text{int}} = 0.175$  mag, which is represented by the dashed curve in the top panel of Figure 6. The solid and dashed curves have been scaled to have the same area. Note that these two distributions are virtually indistinguishable, suggesting that the influence of photometric error on the metallicity distribution function is likely to be negligible.

### 3.6. Metallicity Distribution Function

Now that we have utilized artificial-star experiments to quantify the photometric errors on the RGB, it is possible to use the color of each RGB star to construct a metallicity distribution function (MDF). Figures 3a through 3c show our distance- and reddening-corrected CMDs compared with the RGB fiducials of the Galactic globular clusters

M15, 47 Tuc (both from DCA), and NGC 6553 (Guarnieri et al. 1998), along with the RGB of the open cluster NGC 6791 (Garnavich et al. 1994).

We prefer to use observed cluster fiducials over theoretically calculated RGB sequences because of the uncertainties in the color-temperature calibration and our limited knowledge of the physics of convection. We attempted to make use of the empirical RGB grid constructed by Saviane et al. (2000), but realized that the metallicity range of the grid is not sufficient to cover the range of stars observed in our M31 field. In any case, over the metallicity range common to both RGB sets, there is good agreement between the Saviane et al. (2000) grid and our RGBs discussed below.

The adopted distance moduli and reddenings used to place the cluster fiducials in Figure 3 are given in Table 2. The latter values are taken predominantly from the work of DCA. In the case of NGC 6553, we adopted the reddening advocated by Guarnieri et al. (1998) based on their application of the simultaneous reddening and metallicity method developed by Sarajedini (1994). For NGC 6791, we used an average of the values quoted by Garnavich et al. (1994) and Chaboyer, Green, & Liebert (1999). The distance moduli in Table 2 deserve a more detailed explanation. This is because we utilized a slightly different technique for clusters with RR Lyrae variables as compared with those with red clumps (RCs). To begin with, we note again that our adopted M31 distance modulus is that of Da Costa et al. (2000) and is based on  $M_V(\text{RR}) = 0.17[\text{Fe}/\text{H}] + 0.82$  (Lee, Demarque, & Zinn 1990) for the RR Lyraes. For the three clusters with red clumps, we must modify the calculated  $M_V(\text{RR})$  to take account of the fact that the red clump and the RR Lyraes have different absolute magnitudes and that this magnitude is a function of metallicity and age (Cole 1998; Alves & Sarajedini 1999; Sarajedini 1999; Girardi & Salaris 2001). We consider each of the red clump clusters in turn.

*47 Tuc.*—We make use of the results published by Sarajedini, Lee, & Lee (1995, hereafter SLL), which are based on synthetic HB models that are consistent with our distance scale. From the work of SLL, we see that  $M_V(\text{RC}) = 0.64$ , so that  $(m - M)_V = 13.42$  and thus  $(m - M)_I = 13.37$  for 47 Tuc. This is somewhat smaller than the DCA value of  $(m - M)_V = 13.51$ , which was based on arbitrarily setting the apparent RR Lyrae magnitude of 47 Tuc 0.15 mag fainter than the red clump magnitude. The globular cluster compilation of Harris (1996)<sup>4</sup> gives  $(m - M)_V = 13.37$ .

<sup>4</sup> Available at <http://physun.mcmaster.ca/~harris/mwgc.dat>.

TABLE 2  
ADOPTED CLUSTER PARAMETERS

Cluster	[Fe/H]	$E(V-I)$	$V(\text{HB})^a$	$(m - M)_I$
47 Tuc .....	$-0.71 \pm 0.07$	0.05	14.06	13.37
NGC 1851 .....	$-1.29 \pm 0.07$	0.03	16.05	15.43
M2 .....	$-1.58 \pm 0.06$	0.03	16.05	15.48
NGC 6397 .....	$-1.91 \pm 0.14$	0.23	12.90	12.18
M15 .....	$-2.17 \pm 0.07$	0.13	15.86	15.29
NGC 6553 .....	$-0.28 \pm 0.15$	0.99	16.88	15.18
NGC 6791 .....	$+0.28 \pm 0.18$	0.16	14.55	13.63

<sup>a</sup> All values from Da Costa & Armandroff 1990 except for NGC 6553 (Guarnieri et al. 1998) and NGC 6791 (Sarajedini 1999).

NGC 6553.— Since the age of NGC 6553 is similar to that of 47 Tuc (Zoccali et al. 2001), we need only correct the red clump luminosity of 47 Tuc for the metallicity difference between these two clusters. This correction gives  $M_V(\text{RC}) = 0.71$  so that  $(m - M)_V = 16.17$  and  $(m - M)_I = 15.18$  for NGC 6553. Our values compare favorably with the distance modulus estimated by Guarnieri et al. (1998) of  $(m - M)_V = 15.98 \pm 0.15$ , but differs somewhat from two of the most recent determinations; Zoccali et al. (2001) find  $(m - M)_V = 15.70 \pm 0.13$ , while Beaulieu et al. (2001) derive  $(m - M)_V = 15.4$ .

NGC 6791.—The metal abundance of NGC 6791 is greater than the most metal-rich models presented by SLL. As a result, the corrections for age and metallicity will be performed relative to the  $M_V(\text{RC})$  value of 47 Tuc using the HB models of Girardi et al. (2000; see also Crowl et al. 2001). Thus, because NGC 6791 is 0.99 dex more metal-rich than 47 Tuc and 4 Gyr younger (Chaboyer et al. 1999), we calculate its red clump to be at  $M_V(\text{RC}) = 0.76$ , making its apparent distance moduli equal to  $(m - M)_V = 13.79$  and  $(m - M)_I = 13.63$ . As a comparison, we note that Garnavich et al. (1994) used a modulus of  $(m - M)_V \sim 13.6$  in their study of NGC 6791.

The cluster RGBs shown in Figure 3 are used to calibrate the dereddened RGB color at  $M_I = -2$   $[(V - I)_{0,-2}]$  as a function of  $[\text{Fe}/\text{H}]$ . This magnitude level was chosen to minimize the effects of asymptotic giant branch stars, while at the same time maximizing the effects of metallicity on color. The weighted least-squares relation shown in the bottom panel of Figure 7 is given by

$$[\text{Fe}/\text{H}] = -27.24 + 46.18(V - I)_0 - 26.49(V - I)_0^2 + 5.16(V - I)_0^3. \quad (1)$$

The root mean square deviation of the points from the relation is 0.03 dex. The top panel of Figure 7 shows the metallicity dispersion introduced by the color error of  $\sigma_{\text{err}} = 0.049$  at  $M_I = -2$ . This figure indicates that the photometric error translates to a typical error of only  $\sim 0.2$  dex in metallicity. Furthermore, for NGC 6553, which has the most uncertain distance modulus among the clusters in Table 2, an uncertainty of 0.2 mag in  $(m - M)_I$  also leads to a metallicity error of  $\sim 0.2$  dex.

To construct the MDF, we take the dereddened color of each star within  $\pm 0.1$  mag of  $M_I = -2$  and convert it to a metal abundance using equation (1). In addition, the photometric error is converted to  $\sigma_{[\text{Fe}/\text{H}]}$ . A generalized histogram of the metallicities is then constructed by adding up the unit Gaussians representing the abundance of each star. The resultant MDF of the 271 stars in this magnitude range is shown in the top panel of Figure 8, wherein the filled circles and the solid line are the binned and generalized histograms, respectively. This comparison helps to illustrate which features are significant and which are diluted by the photometric errors. In this regard, we see that the MDF displays a prominent peak at  $[\text{Fe}/\text{H}] \sim -0.1$ , a possible secondary peak at  $[\text{Fe}/\text{H}] \sim -0.7$ , and an extended tail to the metal-poor regime. The bottom panel of Figure 8 displays the effect on the MDF of changing the adopted reddening by  $\pm 0.02$  mag in  $E(B - V)$ . We note that the location of the peak changes by less than 0.1 dex and the overall shape of the MDF remains largely unchanged.

We pointed out earlier that we have neglected differential reddening along the line of sight caused by dust internal to

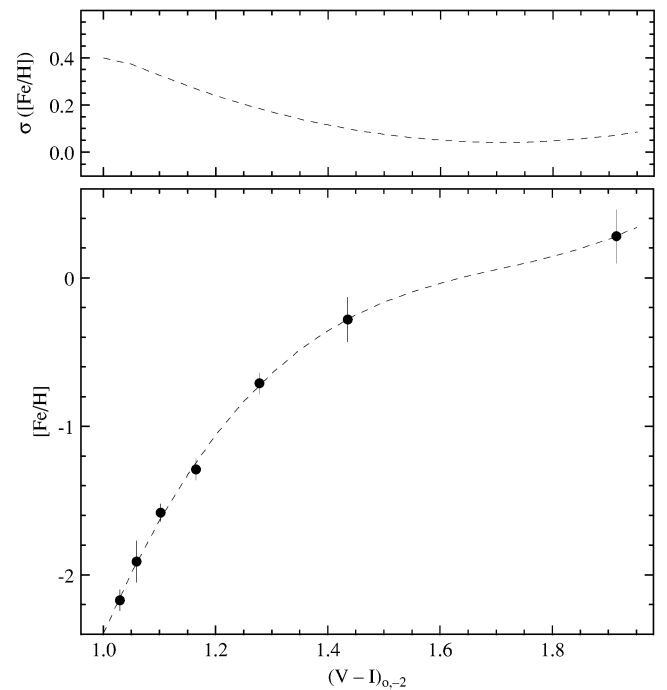


FIG. 7.—*Bottom*: Our relation between the dereddened RGB color at  $M_I = -2[(V - I)_{0,-2}]$  and metal abundance. The filled circles are the star clusters listed in Table 2, while the dashed curve is the weighted least-squares fit shown in eq. (1). *Top*: In light of the photometric error yielded by the artificial stars of  $\sigma_{\text{err}} = 0.049$  mag, metallicity uncertainty resulting purely from the photometric errors.

M31. Taking out this effect will tend to reduce the range of metallicities present in our MDF, and it could systematically lower the higher metallicity measurements. Because it is difficult to precisely account for this, the reader should keep this possibility in mind as the results of the analysis are presented.

### 3.7. Comparison with Other MDFs

Figure 9 shows the MDF for our M31 field (G272) located at a projected radial distance of 23.9 compared with the M31 field halo MDFs from Holland et al. (1996, G302) and Durrell et al. (1994, 2001). These are located at projected radial distances of 32', 40', and 90', respectively, and have been scaled to have the same area as the G272 field. In addition, we have shifted the Durrell et al. (2001) MDF by  $-0.3$  in metal abundance to account for the fact that they quote  $[M/\text{H}]$  rather than  $[\text{Fe}/\text{H}]$  (P. Durrell 2001, private communication).

There are a number of features to note in Figure 9. First, all of the MDFs share the same overall shape; they feature a prominent peak at the metal-rich end with an extended tail to more metal-poor regimes. Relative to the peak, this tail appears to be most prominent in the Holland et al. (1996) and Durrell et al. (2001) MDFs and less so in the Durrell et al. (1994) distribution. Second, the metallicity of the G272 peak occurs at  $[\text{Fe}/\text{H}] \sim -0.1$ , which is significantly more metal-rich than those of the other MDFs (see also Mould & Kristian 1986; Pritchett & van den Bergh 1988).

Another way in which we can intercompare these MDFs is to scale them so that their metal-poor tails match, as shown in the bottom panel of Figure 9. Keeping in mind that the three dashed MDFs are predominantly halo stars

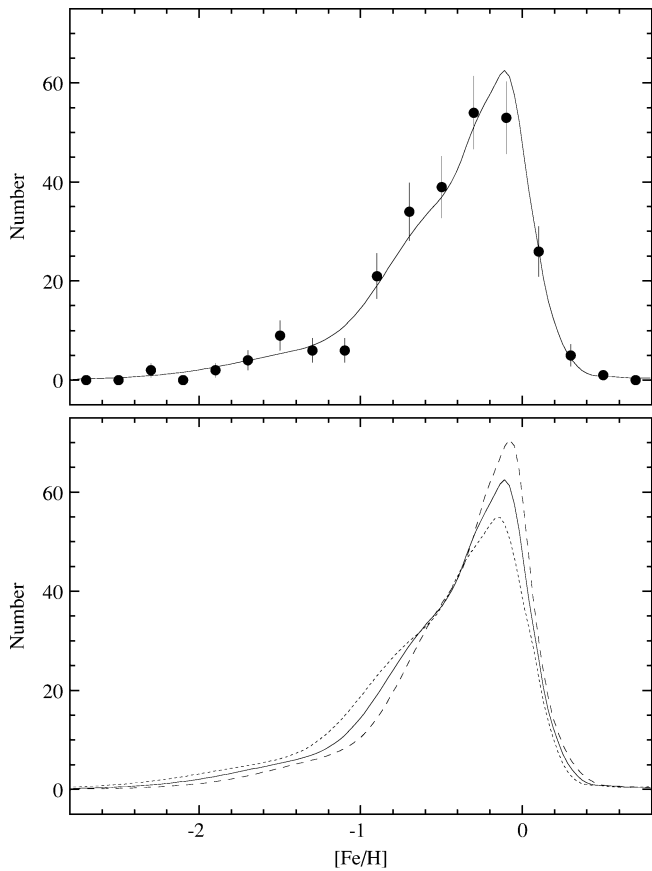


FIG. 8.—Using the dereddened colors of all stars with magnitudes in the range  $22.55 \leq I \leq 22.75$  ( $-1.9 \leq M_I \leq -2.1$ ) along with eq. (1), we construct the metallicity distribution function shown in the top panel by the filled symbols. The solid line is the generalized histogram of these abundances, which takes into account the metallicity error of each star. The bottom panel shows the variation of the MDF as the adopted reddening is varied from  $E(B-V) = 0.06$  (dashed line) to 0.08 (solid line) to 0.10 (dotted line).

in M31, we find that the peak of the halo MDF is consistent with the “secondary peak” at  $[\text{Fe}/\text{H}] \sim -0.7$  in the G272 distribution. This suggests that the latter population contains not just halo stars but also a significant population from another component. We tentatively assign this population to the thick disk of M31, an assertion that is not unrealistic judging from the physical location of our field in M31 (Fig. 1a). Furthermore, we note that, because M31 halo populations do not exhibit a radial abundance gradient for  $R \gtrsim 5$  kpc (van den Bergh 1999), it is unlikely to be the case that the dominant population in the G272 field is simply a higher metallicity halo. Additionally, based on the discussion presented by Durrell et al. (2001), there is the possibility that the metal-rich component in our field is actually the bulge of M31. However, given that the central regions of the bulge are around solar metallicity (Renzini 1999; Jablonka et al. 1999, 2000) and that the mean abundance is expected to decrease at the rate of  $\sim 0.1$  dex  $\text{kpc}^{-1}$  (Durrell et al. 2001), we should expect a peak bulge metallicity of about  $-0.6$  dex at the location of our field. If present, this population would be indistinguishable from our secondary peak at  $[\text{Fe}/\text{H}] \sim -0.7$ .

We can quantify our claim that the metal-rich peak in our MDF belongs to the M31 thick disk by fitting multiple Gaussian distributions to the G272 MDF representing the

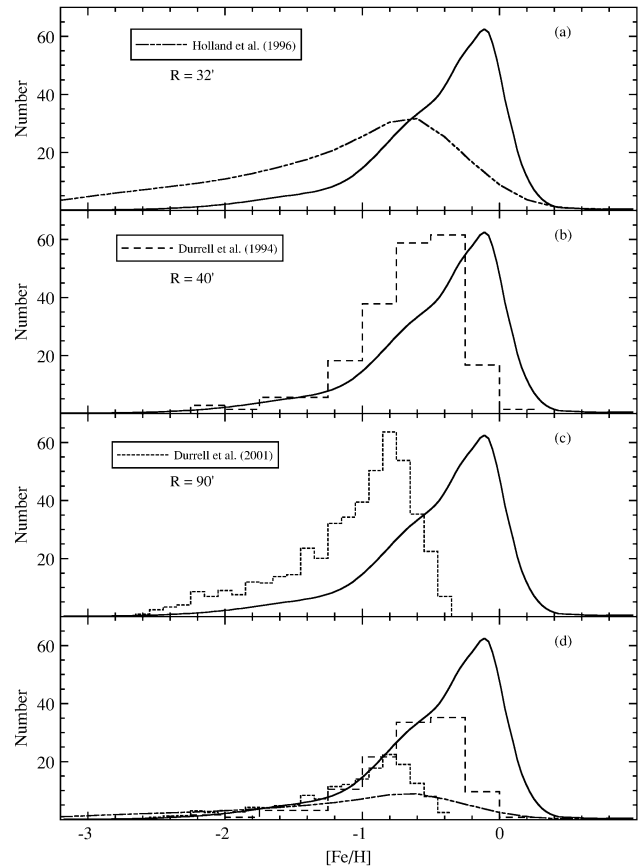


FIG. 9.—(a) Comparison of the G272 field metallicity distribution function (MDF) and that of the G302 field from Holland et al. (1996) located at a projected distance of 32' from the center of M31. (b) Same as (a) except that the MDF of the M31 halo field from Durrell et al. (1994) located at 40' from the nucleus is shown. (c) Same as (a) except that the MDF of the M31 halo field located at 90' from the nucleus and studied by Durrell et al. (2001) is shown. All of these distributions have been scaled to have the same area. (d) The MDFs have been scaled to match the metal-poor tail of the G272 MDF.

three populations that appear to be present—metal-poor and intermediate-metallicity components that belong to the M31 halo and a metal-rich component that may be the thick disk. For the first two populations, we adopt the Gaussian parameters in Table 3 of Durrell et al. (2001). We can then fit a third Gaussian to our MDF to solve for the metallicity parameters (peak and width) of the M31 thick disk. The two panels of Figure 10 illustrate the results of this exercise, with the top panel showing the fit to the binned histogram and the bottom panel displaying the fit to the generalized histogram (see Fig. 8). There is relatively good agreement between the fitted data and the fits, as well as between the fits to the binned and generalized histograms. This procedure suggests a mean metallicity of  $\langle [\text{Fe}/\text{H}] \rangle = -0.22 \pm 0.26$  for the M31 thick disk comprising 70% of the stars in this field. This is in contrast with the abundances of the metal-poor and intermediate-metallicity peaks of  $[\text{Fe}/\text{H}] = -1.50 \pm 0.45$  (10%) and  $[\text{Fe}/\text{H}] = -0.82 \pm 0.20$  (20%), respectively, from Table 3 of Durrell et al. (2001) adjusted by  $-0.3$  dex.

At this point, we return momentarily to the metallicities of the HB and red clump populations. We speculate that the most metal-poor component with  $[\text{Fe}/\text{H}] \sim -1.5$  is likely to be associated with the above-mentioned Population II

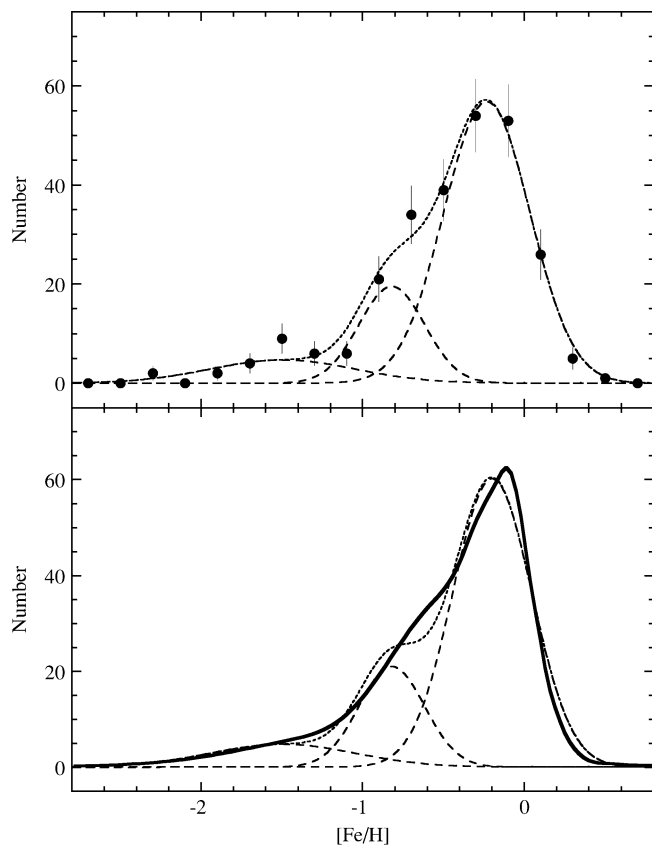


FIG. 10.—Gaussian fits to our metallicity distribution function after adopting the Durrell et al. (2001) parameters for the metal-poor and intermediate-metallicity halo components. The top and bottom panels show the fits to the binned (*filled circles*) and generalized (*solid line*) histograms, respectively. The dashed lines are the individual Gaussian components while the dotted line is the sum of all three.

HB, while the most metal-rich population with  $[\text{Fe}/\text{H}] \sim -0.2$  is probably producing the strong red clump. However, the location of the helium-burning stars associated with the intermediate-metallicity ( $[\text{Fe}/\text{H}] \sim -0.8$ ) component is unclear.

In Figure 11, we compare the G272 MDF with those of the Milky Way's thick-disk stars (Wyse & Gilmore 1995), field halo stars (Ryan & Norris 1991), globular clusters (Harris 1996), and M31's globular clusters (Barmby et al. 2000). Interestingly, the G272 field resembles the Milky Way's thick-disk stars more than it does any of the other halo components (e.g., M31 globulars). One interpretation of this would be that the stellar population of the G272 field is dominated by the thick disk of M31, an assertion that would support our conclusion based on the comparisons in Figure 9 above. However, this is a spurious line of reasoning, because if we follow it to its logical end it implies that the Durrell et al. (2001) MDF (of the M31 outer halo) does not represent the M31 halo because it does not resemble the MDF of the Milky Way halo field stars in Figure 11b.

### 3.8. Age of the Field Population

Further evidence of our assertion that the G272 field is dominated by M31 thick-disk stars can be obtained by examining the age structure of this field. Figure 12 shows the same CMDs as Figure 3, with solar abundance ( $Z = 0.019$ ) isochrones of  $10^8$ ,  $6.3 \times 10^8$ ,  $10^9$ , and  $1.6 \times 10^9$

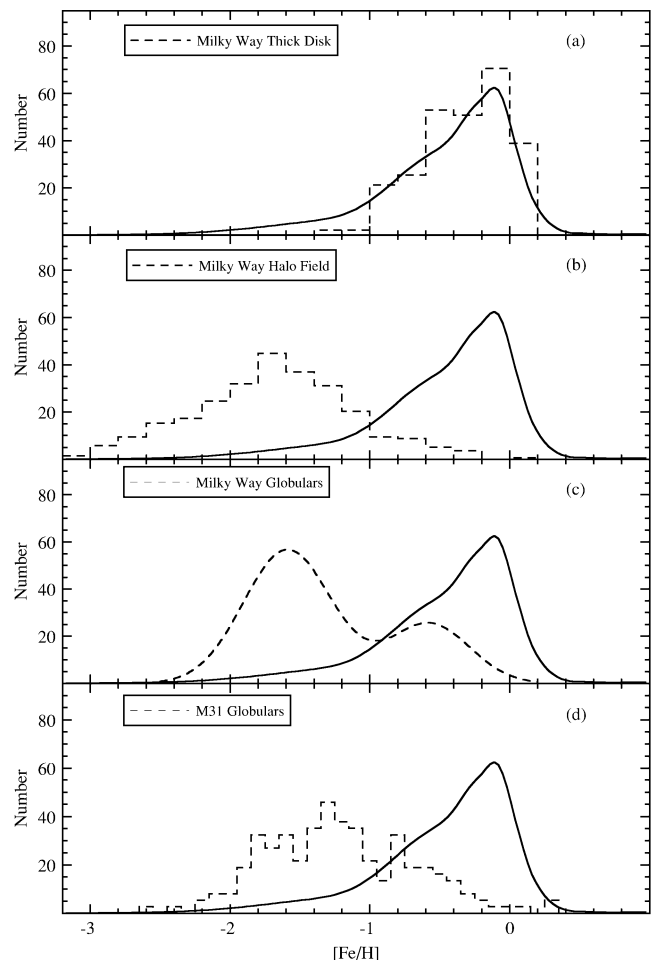


FIG. 11.—(a) Comparison of the G272 field metallicity distribution function (MDF) with that of Milky Way thick-disk stars from Wyse & Gilmore (1995). (b) Same as (a) except that the MDF of Milky Way field halo stars from Ryan & Norris (1991) is shown. (c) Same as (a) except that the MDF of Milky Way Globular clusters constructed from the database of Harris (1996) is shown. (d) Same as (a) except that the MDF of M31 globular clusters from Barmby et al. (2000) is shown. All of these distributions have been scaled to have the same area.

yr (Girardi et al. 2000) overplotted. From these comparisons, we note that the fraction of the stellar population younger than  $10^9$  yr is very small, comparable with the appearance of the G302 field CMD in Holland et al. (1996). In contrast, the observations of M31's disk presented by Williams & Hodge (2001) reveal a significantly larger population of stars with ages younger than  $10^9$  yr. This difference suggests that the contribution of the M31 thin disk to the G272 field is minimal. This, coupled with the fact that the dominant population in the G272 field is likely to be  $\gtrsim 1.5$  Gyr old, provides further circumstantial evidence that the G272 field is probably dominated by intermediate- to old-age thick-disk stars.

## 4. SUMMARY AND CONCLUSIONS

We present the deepest *HST*/WFPC2 photometry of a field in M31. The *VI* color-magnitude diagram is based on 3800 s of exposure time in the F555W filter and 10,800 s in the F814W filter. After adopting a distance of  $(m - M)_0 = 24.5$  and a reddening of  $E(B - V) = 0.08$ , we draw the following conclusions.

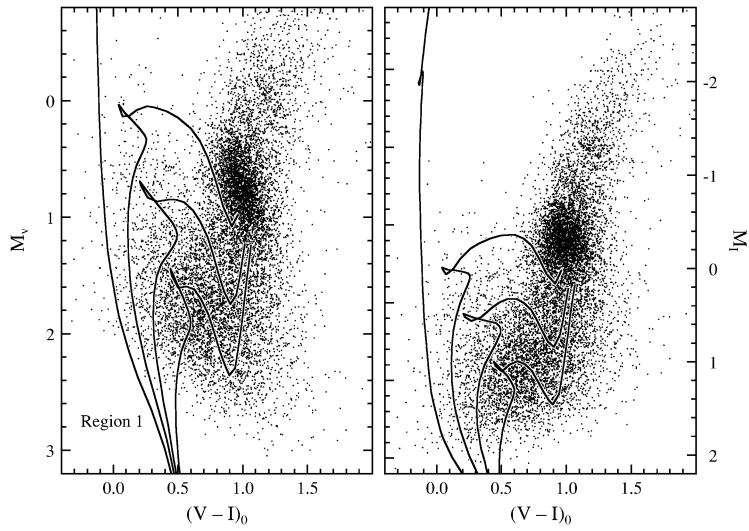


FIG. 12a

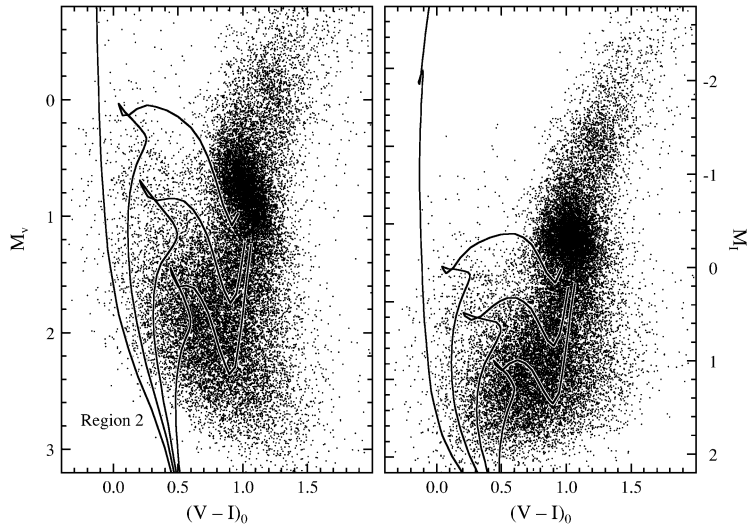


FIG. 12b

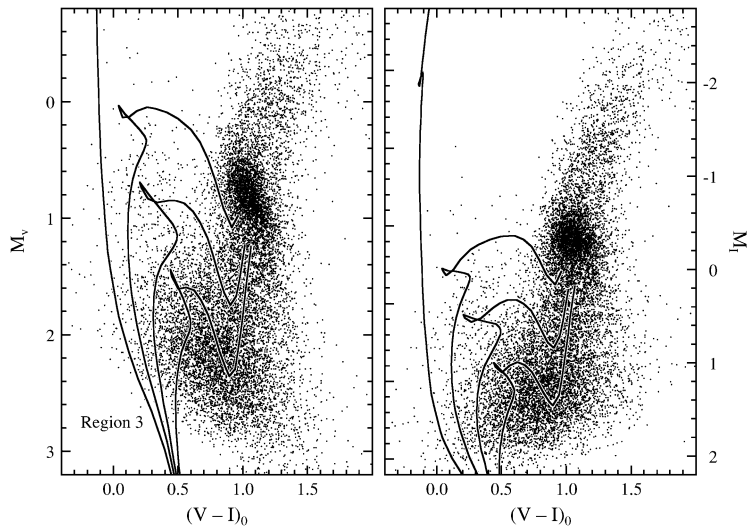


FIG. 12c

FIG. 12.—(a) Left panel shows the distance and reddening corrected  $[M_v, (V-I)_0]$  color-magnitude diagram (CMD) for region 1; the right panel shows the  $[M_I, (V-I)_0]$  CMD. The solid lines are the Girardi et al. (2000) solar abundance ( $Z = 0.019$ ) theoretical isochrones for ages of  $10^8$ ,  $6.3 \times 10^8$ ,  $10^9$ , and  $1.6 \times 10^9$  yr. (b) Same as (a) except that the region 2 CMDs are shown. (c) Same as (a) except that the region 3 CMDs are shown.

1. The *I*-band absolute magnitude of the helium-burning red clump stars is  $M_I(\text{RC}) = -0.29 \pm 0.05$ , which is in accord with the value derived from *Hipparcos* parallaxes of solar neighborhood clump stars by Stanek & Garnavich (1998).

2. The *V*-band absolute magnitude of the asymptotic giant branch (AGB) clump stars is  $M_V(\text{AGB}) = -0.10 \pm 0.07$ ; coupled with the red clump luminosity, this value is consistent with those predicted by the models of Alves & Sarajedini (1999) for an intermediate-age metal-rich population.

3. The metallicity distribution function constructed from bright RGB stars shows a characteristic shape with a prominent peak at  $[\text{Fe}/\text{H}] \sim -0.1$  and an extensive tail to metal-poor regimes as low as  $[\text{Fe}/\text{H}] \sim -2.5$ .

4. A pure halo population consisting of metal-poor and intermediate-metallicity components (Durrell et al. 2001) is not sufficient to account for the shape of our MDF. Instead, an additional Gaussian component with  $\langle[\text{Fe}/\text{H}]\rangle = -0.22 \pm 0.26$ , comprising 70% of the total number of stars, is required.

5. A comparison of our CMD with the theoretical isochrones of Girardi et al. (2000) indicates that the majority of stars in our M31 field have ages older than  $\sim 1.5$  Gyr.

6. All of the above points, along with the physical location of our field in M31, suggest that we have observed the thick-disk population of this galaxy.

We close by emphasizing the need for a robust model describing the spatial distribution of the various M31 components (e.g., thin disk, thick disk, bulge, halo). It is difficult for us to draw more compelling conclusions about the stellar populations of M31 without such a model.

We are grateful to Pat Durrell, Rupali Chandar, Andy Stephens, and Pascale Jablonka for helpful comments on an early version of this manuscript. The suggestions of an anonymous referee also helped to clarify the presentation tremendously. This project has benefited from financial support from NSF CAREER grant AST 00-94048.

## REFERENCES

- Alves, D., & Sarajedini, A. 1999, *ApJ*, 511, 225
- Barmby, P., Huchra, J. P., Brodie, J. P., Forbes, D. A., Schroder, L. L., & Grillmair, C. J. 2000, *AJ*, 119, 727
- Beaulieu, S., Gilmore, G., Elson, R. A. W., Johnson, R. A., Santiago, B., Sigurdsson, S., & Tanvir, N. 2001, *AJ*, 121, 2618
- Bellazzini, M., Ferraro, F., & Pancino, E. 2001, *ApJ*, 556, 635
- Bica, E., Barbuy, B., & Ortolani, S. 1991, *ApJ*, 382, L15
- Bullock, J. 1999, Ph.D. thesis, Univ. California, Santa Cruz
- Burstein, D., & Heiles, C. 1982, *AJ*, 87, 1165
- Caputo, F., Castellani, V., Chieffi, A., Pulone, L., & Tornambè, A. 1989, *ApJ*, 340, 241
- Castellani, V., Chieffi, A., & Pulone, L. 1991, *ApJS*, 76, 911
- Chaboyer, B., Green, E. M., & Liebert, J. 1999, *AJ*, 117, 1360
- Cole, A. 1998, *ApJ*, 500, L137
- Crowl, H. H., Sarajedini, A., Piatti, A., Geisler, D., Bica, E., Clará, J. J., & Santos, J. F. C. 2001, *AJ*, 122, 220
- Cuillandre, J.-C., Lequeux, J., Allen, R. J., Mellier, Y., & Bertin, E. 2001, *ApJ*, 554, 190
- Da Costa, G. S., & Armandroff, T. E. 1990, *AJ*, 100, 162
- Da Costa, G. S., Armandroff, T. E., Caldwell, N., & Seitzer, P. 2000, *AJ*, 119, 705
- Davidge, T. J. 1993, *ApJ*, 409, 190
- Durrell, P. R., Harris, W. E., & Pritchett, C. J. 1994, *AJ*, 108, 2114
- . 2001, *AJ*, 121, 2557
- Ferraro, F. 1992, *Mem. Soc. Astron. Italiana*, 63, 491
- Ferraro, F. R., Messineo, M., Fusi Pecci, F., de Palo, M. A., Straniero, O., Chieffi, A., & Limongi, M. 1999, *AJ*, 118, 1738
- Fusi Pecci, F., Ferraro, F. R., Crocker, D. A., Rood, R. T., & Buonanno, R. 1990, *A&A*, 238, 95
- Fusi Pecci, F., et al. 1996, *AJ*, 112, 1461
- Gallart, C. 1998, *ApJ*, 495, L43
- Garnavich, P. M., VandenBerg, D. A., Zurek, D. R., & Hesser, J. E. 1994, *AJ*, 107, 1097
- Girardi, L., & Salaris, M. 2001, *MNRAS*, 323, 109
- Girardi, L., Bressan, A., Bertelli, G., & Chiosi, C. 2000, *A&AS*, 141, 371
- Grebel, E. K. 2000, in *ASP Conf. Ser. 239, A New Era of Microlensing Astrophysics*, ed. J. W. Menzies & P. D. Sackett (San Francisco: ASP), 262
- Guarnieri, M. D., Ortolani, S., Montegriffo, P., Renzini, A., Barbuy, B., Bica, E., & Moneti, A. 1998, *A&A*, 331, 70
- Harris, W. E. 1996, *AJ*, 112, 1487
- Hodge, P., & Lee, M. -G. 1988, *ApJ*, 329, 651
- Hodge, P., Lee, M. -G., & Mateo, M. 1988, *ApJ*, 324, 172
- Holland, S., Fahlman, G., & Richer, H. 1996, *AJ*, 112, 1035
- Jablonka, P., Bridges, T., Sarajedini, A., Meylan, G., Maeder, A., & Meynet, G. 1999, *ApJ*, 518, 627
- Jablonka, P., Courbin, F., Meylan, G., Sarajedini, A., Bridges, T. J., & Magain, P. 2000, *A&A*, 359, 131
- Johnson, J., & Bolte, M. 1998, *AJ*, 115, 693
- Layden, A. C., & Sarajedini, A. 1997, *ApJ*, 486, L107
- Lee, Y. -W., Demarque, P., & Zinn, R. J. 1990, *ApJ*, 350, 155
- Massey, P., Armandroff, T. E., & Conti, P. S. 1986, *AJ*, 92, 1303
- Morris, P. W., Reid, I. N., Griffiths, W. K., & Penny, A. J. 1994, *MNRAS*, 271, 852
- Mould, J. R., & Kristian, J. 1986, *ApJ*, 305, 591
- Pritchett, C. J., & van den Bergh, S. 1988, *ApJ*, 331, 135
- Renzini, A. 1999, in *When and How Do Bulges Form and Evolve?* ed. C. M. Carollo, H. C. Ferguson, & R. F. G. Wyse (Cambridge: Cambridge Univ. Press), 9
- Rich, R. M., Mighell, K., & Neill, J. D. 1996, in *ASP Conf. Ser. 92, Formation of the Galactic Halo... Inside and Out*, ed. H. Morrison & A. Sarajedini (ASP: San Francisco), 544
- Richer, H. B., Crabtree, D. R., & Pritchett, C. J. 1990, *ApJ*, 355, 448
- Ryan, S. G., & Norris, J. E. 1991, *AJ*, 101, 1865
- Sakai, S., Zaritsky, D., & Kennicutt, R. C., Jr. 2000, *AJ*, 119, 1197
- Sarajedini, A. 1994, *AJ*, 107, 618
- . 1999, *AJ*, 118, 2321
- Sarajedini, A., & Forrester, W. L. 1995, *AJ*, 109, 1112
- Sarajedini, A., Geisler, D., Schommer, R., & Harding, P. 2000, *AJ*, 120, 2437
- Sarajedini, A., Lee, Y. -W., & Lee, D. -H. 1995, *ApJ*, 450, 712
- Saviane, I., Rosenberg, A., Piotto, G., & Aparicio, A. 2000, *A&A*, 355, 966
- Schlegel, D. J., Finkbeiner, D. P., & Davis, M. 1998, *ApJ*, 500, 525
- Silbermann, N. A., et al. 1996, *ApJ*, 470, 1
- Silk, J. 2001, *MNRAS*, 324, 313
- Stanek, K. Z., & Garnavich, P. M. 1998, *ApJ*, 503, L131
- Stetson, P. B. 1994, *PASP*, 106, 250
- van den Bergh, S. 1999, *A&A Rev.*, 9, 273
- Walker, A. 1994, *AJ*, 108, 555
- Williams, B. F., & Hodge, P. 2001, *ApJ*, 548, 190
- Wyse, R., & Gilmore, G. 1995, *AJ*, 110, 2771
- Zoccali, M., Renzini, A., Ortolani, S., Bica, E., & Barbuy, B. 2001, *AJ*, 121, 2638